Dispersive magnetic excitations in the $S=1$ antiferromagnet $Ba_3Mn_2O_8$

M. B. Stone,[1] M. D. Lumsden,[1] Y. Qiu,[2,3] E. C. Samulon,[4] C. D. Batista,[5] and I. R. Fisher[4]

[1]*Neutron Scattering Science Division, Oak Ridge National Laboratory, Oak Ridge, Tennessee 37831, USA*
[2]*NIST Center for Neutron Research, Gaithersburg, Maryland 20899, USA*
[3]*Department of Materials Science and Engineering, University of Maryland, College Park, Maryland 20742, USA*
[4]*Department of Applied Physics and Geballe Laboratory for Advanced Materials, Stanford University, California 94305, USA*
[5]*Theoretical Division, Los Alamos National Laboratory, Los Alamos, New Mexico 87545, USA*

We present powder inelastic neutron scattering measurements of the $S=1$ dimerized antiferromagnet $Ba_3Mn_2O_8$. The $T=1.4$ K magnetic spectrum exhibits a spin gap of $\Delta \approx 1.0$ meV and a dispersive spectrum with a bandwidth of approximately 1.5 meV. A comparison to coupled dimer models accurately describes the dispersion and scattering intensity and determines the exchange constants in $Ba_3Mn_2O_8$. The wave vector dependent scattering intensity confirms the proposed $S=1$ dimer bond. Temperature dependent measurements of the magnetic excitations indicate the presence of both singlet-triplet and thermally activated triplet-quintet excitations.

PACS number(s): 75.10.Jm, 75.40.Gb, 75.30.Et

I. INTRODUCTION

Low-dimensional and gapped quantum magnets based on strongly coupled spin pairs or dimers with weaker interdimer interactions have become especially topical systems. This is primarily due to the relevance of experimentally accessible quantum critical points.[1–4] For antiferromagnetic intradimer exchange, the ground state of such systems is a product of singlets, but strong magnetic fields can close the spin gap to excited triplet states via Zeeman splitting of the triplet.[5–7] Such systems thus provide an elegant realization of a lattice gas of hard core bosons in which the external magnetic field plays the role of the chemical potential and the interdimer coupling determines both the kinetic and potential energy of the delocalized triplets.[8,9] Depending on the balance of these energy scales, the triplets will either crystallize or condense at low temperatures[10] or, under the right set of conditions, form a supersolid.[11] $Ba_3Mn_2O_8$ is a particularly promising candidate material for the detailed study of magnetic field dependent quantum critical points. $Ba_3Mn_2O_8$ has been identified as a $S=1$ dimerized antiferromagnet and the low-temperature phase diagram has been examined using thermodynamic measurements.[12–14] However, a measure of the dominant exchange constants has been notably absent.

Low-field magnetic susceptibility and pulsed field magnetization measurements of $Ba_3Mn_2O_8$ agree with weakly coupled $S=1$ dimer models with antiferromagnetic dimer exchange J_0 between 1.50 and 1.65 meV and a zero-field spin gap of $\Delta=0.97$ meV.[12,15] Unfortunately, comparisons to isolated dimer models only yield results in terms of weighted sums of interdimer exchange. Specific heat measurements on powder samples have been performed in magnetic fields up to $\mu_0 H = 29$ T to describe the low-temperature magnetic phase diagram of $Ba_3Mn_2O_8$.[13] At $T \approx 0.6$ K, a critical field of $\mu_0 H \approx 11$ T is required to induce magnetic ordering. Following the thermodynamic phase transition to lower temperatures, the experiments extrapolate to a zero-temperature $\mu_0 H_{c1} = 9.04(0.15)$ T quantum critical point. These measurements also indicate two phase transitions near the lower criti-

cal field, implying the existence of two magnetic long-range-ordered phases in close proximity to the quantum critical point.

More recent measurements using single crystals confirm the presence of two distinct ordered phases and provide a detailed map of the phase diagram.[14] EPR measurements indicate a zero-field splitting of the triplet states, attributed in part to the effects of single-ion anisotropy[16] and implying more complex magnetic structures than previously suggested.[15]

The applicable Hamiltonian for this system is not yet fully characterized, and the magnitude and extent of dimer and interdimer exchange interactions are important for a further
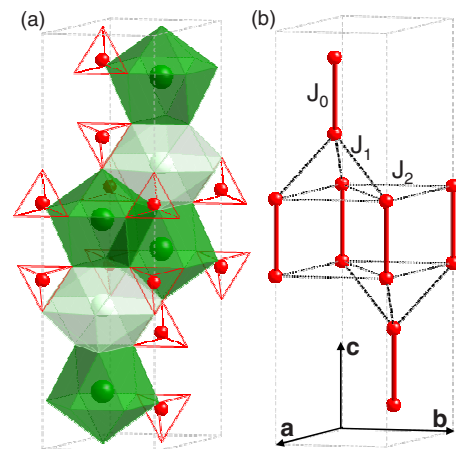

FIG. 1. (Color online) Crystal structure of $Ba_3Mn_2O_8$. Oxygen atoms are not shown for clarity. Gray dashed lines indicate chemical unit cells. (a) Polyhedral representation of structure. Light green and dark green polyhedra around Ba sites represent the two types of Ba coordination that alternate along the c axis, 12-fold and 10-fold coordination, respectively. Red tetrahedra illustrate the Mn^{5+} coordination. (b) Simplified structure figure illustrating dominant exchange connectivity in $Ba_3Mn_2O_8$ within and between the $S=1$ dimers. J_1 and J_2 exchanges correspond to distances of 4.569 and 5.711 Å, respectively.

understanding of $Ba_3Mn_2O_8$ in both zero and applied magnetic fields. Here, we describe temperature dependent inelastic neutron scattering (INS) measurements on polycrystalline samples to determine the extent of dispersive magnetic excitations and exchange constants in $Ba_3Mn_2O_8$.

$Ba_3Mn_2O_8$ is hexagonal (with the space group $R\bar{3}m$) with room-temperature lattice constants $a=5.711$ and $c=21.444$ Å.[18] The Mn^{5+} ions reside in a distorted tetrahedral environment, as shown in Fig. 1(a), resulting in an effective $S=1$ moment. Dimer and interdimer magnetic interactions are considered to be antiferromagnetic ($J>0$) and Heisenberg with a small single-ion anisotropy, D. Including a Zeeman term for applied magnetic fields H along the z axis, the Hamiltonian is

$$\mathcal{H} = \sum_{i,j} \frac{J_{i,j}}{2} \mathbf{S}_i \cdot \mathbf{S}_j + D\sum_i (S_i^z)^2 - g\mu_B H \sum_i S_i^z, \quad (1)$$

where i and j denote coordinates of individual interacting spins S. The nearest neighbor $S=1$ sites along the c axis, $d=3.985$ Å, have been proposed as strongly coupled antiferromagnetic $S=1$ dimers. The dimers form an edge-sharing triangular lattice bilayer in the ab plane. Neighboring planes along the c axis are separated by alternating layers of oxygen coordinated Ba sites, 10 and 12 site coordinations, as illustrated in Fig. 1(a). Weaker interdimer exchanges within the ac plane, J_2, and between the bilayers, J_1, have also been proposed based on the crystal structure. These are illustrated in Fig. 1(b) along with the dimer exchange J_0.

II. EXPERIMENTAL METHODS

Powder samples of $Ba_3Mn_2O_8$ were synthesized using stoichiometric amounts of $BaCO_3$ and Mn_2O_3 in a solid state reaction. The reactants were calcined under flowing oxygen at 900 °C for 30 h. The resulting green powder was then reground and sintered between 900 and 1000 °C under flowing oxygen for approximately 7 days. This growth procedure is similar to that described in Ref. 12. Single crystals of appropriate mass are unfortunately not yet available for studies of the dispersion using INS.

Superconducting quantum interference device (SQUID) magnetization measurements as a function of temperature for $\mu_0 H=1000$ T and as a function of magnetic field for $T=40$ K did not reveal any measurable impurities due to Mn_2O_3 and Mn_3O_4, which are ferrimagnetic below $T_c=79$ K and antiferromagnetic below $T_c=43$ K, respectively.[19] The temperature dependent magnetic susceptibility compares well with previously published data with a rounded peak at $T=18$ K and an activated low-temperature susceptibility characteristic of antiferromagnetic spin-gap systems.[12,15] We also characterize the $150 \leq T \leq 350$ K magnetic susceptibility via a Curie–Weiss law with $\Theta_{CW}=-43.2(2)$ K.

Inelastic neutron scattering measurements were performed on 76 g of $Ba_3Mn_2O_8$ in an 18 mm diameter and 100 mm tall cylindrical aluminum sample can. The sample was produced from five separately prepared batches of $Ba_3Mn_2O_8$. Each batch was checked for impurity phases us-

ing SQUID magnetization and powder x-ray diffraction. Both measurements found no measurable impurity phases. Inelastic neutron scattering measurements were performed using the direct geometry chopper spectrometer DCS at the NIST Center for Neutron Research. Spectra were measured for temperatures between $T=1.4$ and $T=160$ K for 1 h in each configuration. Temperature control was provided by a liquid ^{4}He flow cryostat. Two incident wavelengths λ were used. $\lambda=2.9$ Å measurements probed energy transfers up to $\hbar\omega=5.5$ meV and wave vectors up to $Q=4.05$ Å^{-1} at the elastic position. $\lambda=4.4$ Å measurements provide improved energy and wave vector resolution up to $\hbar\omega=3.05$ meV and $Q=2.69$ Å^{-1}. The calculated full width at half maximum energy resolution at the elastic position is $\delta\hbar\omega=0.5$ and 0.15 μeV for the 2.9 and 4.4 Å incident wavelengths, respectively. Background measurements were made for each incident wavelength using an empty sample can at $T=1.4$ K. A $T<200$ K vanadium standard was measured for a calibration of detector sensitivity. A scattering angle dependent absorption correction for the cylindrical sample geometry was also applied to the inelastic scattering intensity. Unless otherwise noted, these backgrounds and normalization are applied to our presented results.

Neglecting Bose occupation and Debye–Waller factors, the magnetic neutron-scattering cross section is proportional to the scattering function, $\mathcal{S}(\mathbf{Q},\omega)$,

$$\frac{d^2\sigma}{d\Omega dE'} \propto \frac{k'}{k} |F(Q)|^2 \mathcal{S}(\mathbf{Q},\omega), \quad (2)$$

where k' and k are the magnitude of the final and initial neutron wave vectors and $F(Q)$ is the magnetic ion form factor. We plot our measured scattering intensity in units of $\mathcal{S}(\mathbf{Q},\omega)$, but we do not normalize the data by the magnetic form factor.

III. RESULTS AND DISCUSSION

Figure 2 shows the scattering intensity as a function of wave vector transfer in the vicinity of the elastic position, $-0.1 \leq \hbar\omega \leq 0.1$ meV, at several temperatures. Nuclear Bragg peak positions and intensity compare well with the previously determined room-temperature structure.[18] We note that for $T \leq 80$ K there are two additional weak Bragg peaks at $Q=1.096$ and 1.545 Å^{-1}. These are likely associated with either Mn_2O_3 or Mn_3O_4 impurities as discussed earlier. We do not observe any contribution from spin waves due to these impurities in the inelastic portion of the spectra.

Although wave vector resolution was not optimized for diffraction ($\frac{\delta Q}{Q=1 \text{ Å}} \approx 0.03$ for $\lambda=4.4$ Å), we fit the (003), (006), (009), and (110) Bragg peak positions for each incident wavelength to determine lattice constants as a function of temperature [Figs. 3(a) and 3(b)]. These values are consistent with the previously determined room-temperature structure. There are no apparent structural phase transitions from $T=160$ to 1.4 K. Both the a and c lattice vectors contract at lower temperatures, but there is only a 0.3% change in the a-axis lattice constant and an even smaller change in the c-axis lattice constant, 0.06%, from $T=295$ K to T
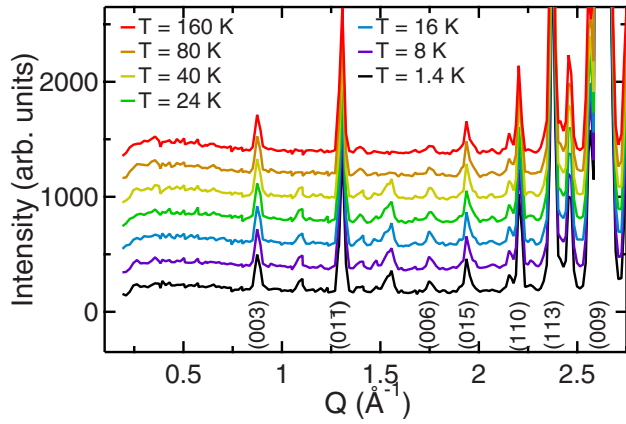
FIG. 2. (Color online) Temperature dependent diffraction for $Ba_3Mn_2O_8$ measured in the $\lambda=2.9$ Å configuration. Data are integrated between -0.1 and 0.1 meV energy transfer. Data have not been background subtracted or corrected for absorption. Higher temperature data are offset vertically from the $T=1.4$ K data for presentation. Several characteristic Bragg peaks are indexed in the figure.

FIG. 3. (Color online) Temperature dependent lattice parameters of $Ba_3Mn_2O_8$. (a) c-axis lattice constant versus temperature. (b) a-axis lattice constant versus temperature. (c) c/a as a function of temperature. Solid points from Ref. 18 for $T=295$ K are shown for comparison. Lattice constants were obtained from the weighted mean peak position of the (003), (006), (009), and (110) Bragg peaks for $\lambda=2.9$ and 4.4 Å. Error bars are the error in the mean. Solid lines in (a) and (b) are linear fits described in the text. The solid line in (c) is calculated based on the linear fits for the a- and c-axis lattice constants.

$=1.4$ K. Linear fits to these data along with the $T=295$ K values are shown in Figs. 3(a) and 3(b) along with calculated values of c/a and the respective calculated curve in panel (c). The fitted lines provide a good description of the data with coefficients of linear expansion: $\alpha_c = \frac{1}{c(T=0)}\frac{dc}{dT} = 2.3(1)E$ -6 K and $\alpha_a = \frac{1}{a(T=0)}\frac{da}{dT} = 1.25(1)E-5$ K^{-1}. Including quadratic terms does not substantially improve the fits. The weak lattice parameter temperature dependence indicates that any changes in the magnetic excitation spectra with temperature are not likely associated with changes in exchange due to changes in distance between individual spins.

The $T=1.4$ K excitation spectra for the $\lambda=4.4$ and 2.9 Å configurations are shown in Figs. 4(a) and 4(b). There is a single dispersive excitation with a gap of $\Delta\approx1$ meV and a bandwidth of approximately 1.5 meV. The decreasing scattering intensity with increasing wave vector transfer immediately suggests that the spectrum is magnetic. The increase in scattering intensity near $\hbar\omega=0.25$ meV in Fig. 4(a) for small wave vectors is not intrinsic to the sample and has been seen in background measurements. Figures 4(e) and 4(f) show the low-temperature wave vector integrated scattering intensity. There is a peak in the magnetic density of states in the vicinity of the spin-gap energy, but there is no peak at the top of the dispersive band of excitations. The spectrum of one-dimensional Heisenberg gapped quantum antiferromagnets has characteristic Van Hove singularities at the top and bottom of the band. The absence of any peak at higher energy transfers implies that the magnetic excitations in $Ba_3Mn_2O_8$ are at least two dimensional in their connectivity.

For comparison to our results, we calculate the INS cross section of $S=1$ antiferromagnetic dimers with weak interdimer interactions. At finite temperatures the scattering function is written as[20]
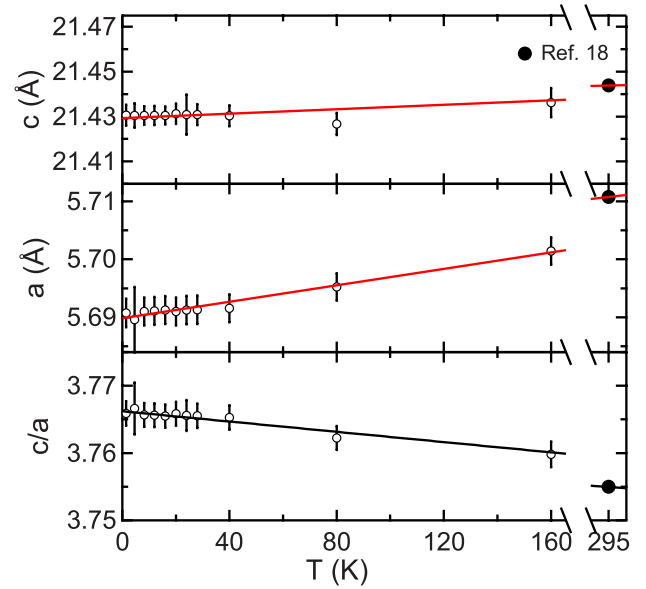
$$S(\mathbf{Q},\omega) = \frac{1}{Z}\sum_{\psi,\psi'} e^{-E_\psi\beta}\sum_j |\langle\psi'|S_j e^{i\mathbf{Q}x_j}|\psi\rangle|^2\delta(E_\psi - E_{\psi'} + \hbar\omega),$$

(3)

where $\beta = \frac{1}{k_B T}$, Z is the partition function, and the sum is over the initial and final states ψ and ψ' with energies E_ψ and $E_{\psi'}$. For a dimer, Eq. (3) becomes

$$S(\mathbf{Q},\omega) = \frac{1}{Z}\sum_{\psi,\psi'} e^{-E_\psi\beta}|\langle\psi'|S_1 e^{i\mathbf{Q}x_1} + S_2 e^{i\mathbf{Q}x_2}$$
$$\times|\psi\rangle|^2\delta(E_\psi - E_{\psi'} + \hbar\omega),$$

(4)

where x_1 and x_2 are the respective crystallographic coordinates of the spins in the dimer and S_n are the spin operators.

An isolated antiferromagnetic $S=1$ dimer with intradimer exchange J_0 will have a nonmagnetic (total spin $S_T=0$) singlet ground state at an energy of $E=-2J_0$ with $S_T=1$ triplet and $S_T=2$ quintet excited states at energies $E=-J_0$ and $E=J_0$. This results in triplet and quintet spin gaps of $\hbar\omega=J_0$ and $\hbar\omega=3J_0$. However, magnetic INS will only probe the singlet-triplet and triplet-quintet cross sections, i.e., $|\Delta S_T| = 1$. Including structure factors from Eq. (4), the scattering function is a sum of two terms,
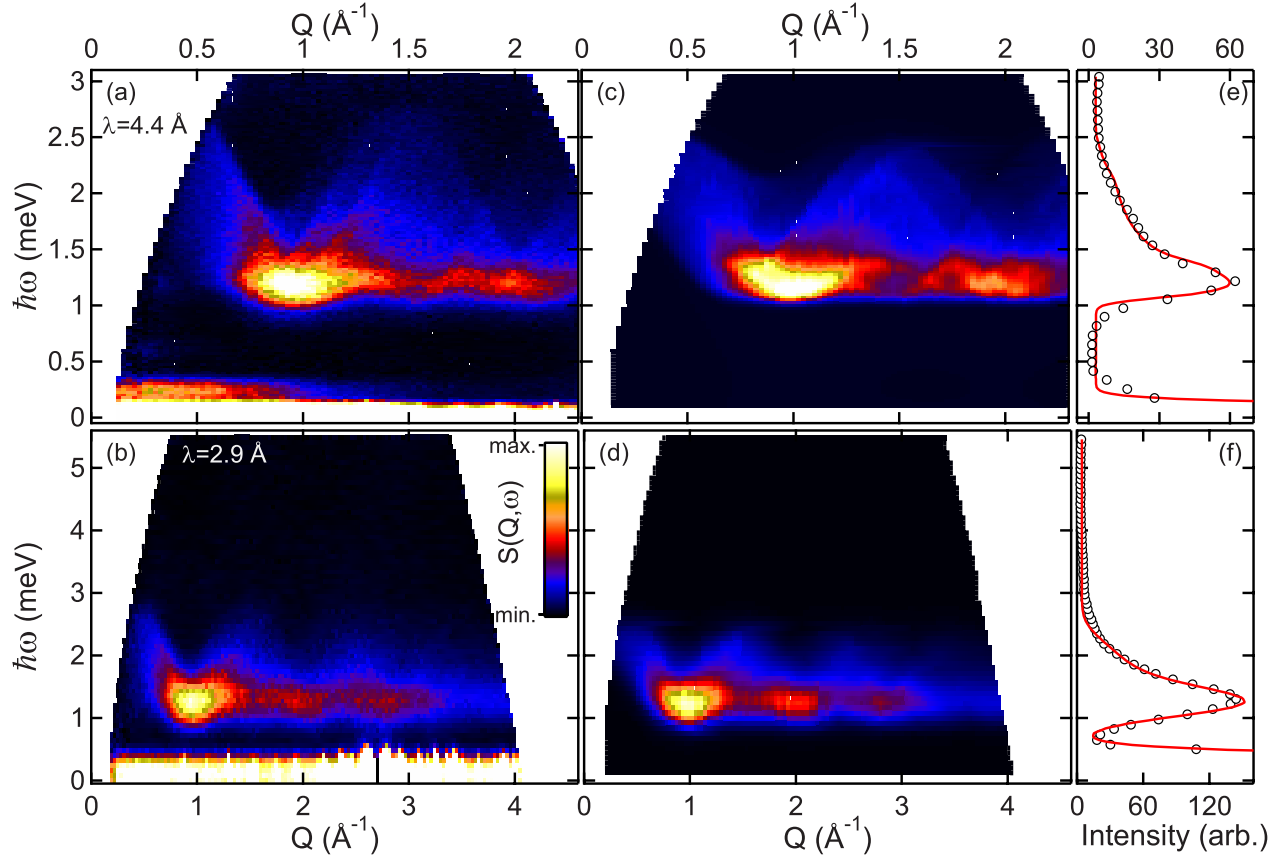
FIG. 4. (Color online) Measured and calculated INS intensity for $Ba_3Mn_2O_8$ at $T=1.4$ K. (a) and (b) are data measured for incident wavelengths of $\lambda=4.4$ and 2.9 Å, respectively. (c) and (d) are the calculated scattering intensities corresponding to the coupled $S=1$ dimer model described in the text. (e) and (f) are the energy dependent integrated scattering intensity of the data and model calculations shown in (a)–(d) for wave vectors $0.65 < Q < 2$ Å^{-1} and $0.75 < Q < 3.25$ Å^{-1} for $\lambda=4.4$ and 2.9 Å, respectively. Model line shapes in (e) and (f) are fitted to the data including an elastic Gaussian line shape and a constant background as discussed in the text.

$$S(\mathbf{Q},\omega) = \frac{4e^{2J\beta}[1-\cos(\mathbf{Q}\cdot\mathbf{d})]}{e^{2J\beta}+3e^{J\beta}+5e^{-J\beta}}\delta(\hbar\omega - J)$$
$$+ \frac{5e^{J\beta}[1-\cos(\mathbf{Q}\cdot\mathbf{d})]}{e^{2J\beta}+3e^{J\beta}+e^{-J\beta}}\delta(\hbar\omega - 3J), \quad (5)$$

where $\mathbf{d}$ is the bond vector between the spins of the dimer. Although the calculated matrix elements of the triplet-quintet transitions are larger than the singlet-triplet transitions, the triplet-quintet transitions are thermally activated with less spectral weight and will only be populated at higher temperatures.

Equation (5) does not account for interdimer correlations, i.e., dispersive excitations. The random phase approximation (RPA) has been successful in describing the dispersion of weakly coupled dimers in spin-gap systems. This has been illustrated for varying numbers of interactions and spin quanta in several experimental systems, including $KCuCl_3$,[21,22] $TlCuCl_3$,[23] $Cs_3Cr_2Br_9$,[24] $Cs_3Cr_2I_9$,[25] $PHCC$,[4] and $BaCuSi_2O_6$.[26] The RPA dispersion for Heisenberg exchange coupled dimers is

$$\hbar\omega(\mathbf{Q}) = \sqrt{\Delta^2 + M^2\Delta\mathcal{J}(\mathbf{Q})R(T)}, \quad (6)$$

where M^2 is the transition matrix element ($M^2 = \frac{4}{3}S[S+1]$), $\mathcal{J}(\mathbf{Q})$ is the Fourier sum over interactions beyond dimer ex-

change, and $\Delta \equiv J_0$ and $R(T)$ is the thermal population difference between the ground and excited states. For $S=1$ antiferromagnetic dimers,

$$R(T) = \frac{1-\exp(-\Delta\beta)}{1+3\exp(-\Delta\beta)+5\exp(-3\Delta\beta)}, \quad (7)$$

considering only singlet-triplet excitations. $Ba_3Mn_2O_8$ has a single dimer per unit cell, and the interdimer interactions propagate the triplet excitation, leading to the Fourier sum

$$\omega_2 = \cos(2\pi k) + \cos(2\pi[h+k]) + \cos(2\pi h),$$

$$\omega_1 = \cos\left(\frac{2\pi}{3}[-h+k+l]\right) + \cos\left(\frac{2\pi}{3}[-h-2k+l]\right)$$
$$+ \cos\left(\frac{2\pi}{3}[2h+k+l]\right),$$

$$\mathcal{J}(\mathbf{Q}) = 2J_2\omega_2 + J_1\omega_1. \quad (8)$$

Recent EPR measurements have revealed a zero-field splitting of $D=-0.032$ meV, although both modes will have an identical dispersion.[16] Examination of thermodynamic measurements have included an exchange constant, J_3, which

couples neighboring dimers in a bilayer from spin 1 of a dimer to spin 2 of a second dimer.[15] This exchange term represents a change in phase of the triplet excitation between dimers in the ab plane and would change the prefactor of the ω_2 term in Eq. (8) to be $2(J_2-J_3)$. We have chosen to omit the J_3 exchange from the current analysis. Because of its large spin-spin distance (6.964 Å) and out of plane coupling, it is presumably much weaker than J_2 and J_1. In addition, recent calculations examining the relative strength of exchange constants in $Ba_3Mn_2O_8$ have shown that the J_3 exchange constant is effectively zero.[17]

The scattering function must also be modified to account for the dispersive excitations. The single mode approximation (SMA) has been successfully applied to several dispersive disordered gapped antiferromagnets with interdimer exchange included in the Hamiltonian.[26–29] This results in an additional multiplicative $\frac{1}{\omega(Q)}$ term in $\mathcal{S}(\mathbf{Q},\omega)$, such that considering only singlet-triplet scattering for $Ba_3Mn_2O_8$ the scattering function becomes

$$\mathcal{S}(\mathbf{Q},\omega) = \frac{4e^{2J\beta}[1-\cos(\mathbf{Q}\cdot\mathbf{d})]}{(e^{2J\beta}+3e^{J\beta}+5e^{-J\beta})\hbar\omega(\mathbf{Q})}\delta[\hbar\omega-\hbar\omega(\mathbf{Q})],$$

(9)

where $\hbar\omega(\mathbf{Q})$ is given by Eqs. (6)–(8). The SMA is appropriate for the case of $Ba_3Mn_2O_8$ for $T\ll J_0$ since only singlet-triplet excitations will be effectively probed via INS in this temperature regime.

For comparison of our high resolution ($\lambda=4.4$ Å) polycrystalline measurements, we numerically *spherically average* Eq. (9),

$$\mathcal{S}(Q,\omega) = \int \frac{d\Omega_{\hat{q}}}{4\pi}\mathcal{S}(\mathbf{Q},\omega).$$

(10)

This process was also recently employed successfully in the examination of polycrstyalline measurements of a gapped antiferromagnet using the same instrumentation.[27] The interpretation of our measurements is more straightforward, given the absence of hydrogen or contamination from phonons in our spectrum. We calculate $\mathcal{S}(\mathbf{Q},\omega)$ over spherical shells in $|\mathbf{Q}|$ space at fixed values of energy transfer, with $\mathbf{d}$ fixed as the proposed dimer bond vector. This was done for a series of J_0, J_1, and J_2 values. This spectrum was combined with an identical spectrum shifted in energy transfer by the value $D=-0.032$ meV. The spectrum was then multiplied by $|F(Q)|^2$ (Refs. 30 and 31) and convolved with a Gaussian representation of the mean instrumental energy and wave vector resolution over the energy and wave vector range of the magnetic excitation. A constant background and a multiplicative prefactor were used as fitting parameters of the calculated spectrum in comparison to the measured data. This procedure yields best fit exchange constants $J_0=1.61(3)$ meV, $J_1=-0.062^{+0.007}_{-0.066}$ meV, and $J_2=0.112^{+0.015}_{-0.003}$ meV.[32] The corresponding best fit INS scattering intensity for both instrument configurations is plotted in Figs. 4(c) and 4(d) and agrees very well with the dispersion and intensity modulation observed in the measurement. The determined value of J_0 and the corresponding spin gap based on the dispersion, Δ
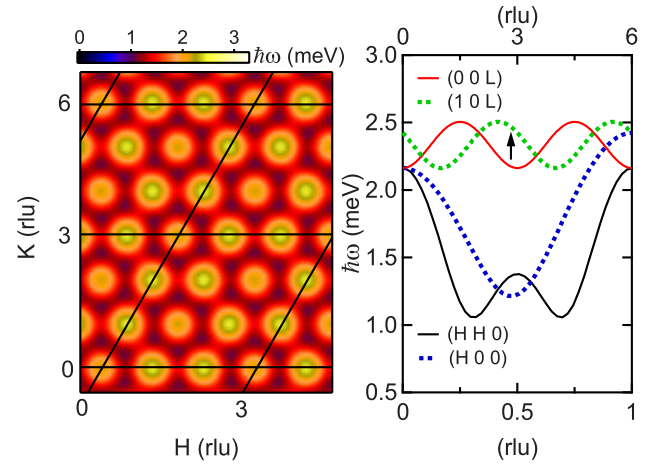

FIG. 5. (Color online) $T=1.4$ K singlet-triplet single crystal dispersion relation determined for $Ba_3Mn_2O_8$ based on powder average analysis. (a) Contour figure of dispersion in the hexagonal (HK0) plane. (b) Dispersion as a function of rlu along other primary directions of the hexagonal structure. Dispersion along the (00L) and (10L) directions is plotted using the top axis.

$=1.05$ meV, are both in the vicinity of values from thermodynamic measurements.

Figures 4(e) and 4(f) show the fitted wave vector integrated line shapes compared to the measured data. Fit parameters for the calculated line shapes include an elastic Gaussian, an overall multiplicative prefactor, and a constant background. The calculations based on both incident wave lengths agree very well with the measurement.

We plot the low-temperature singlet-triplet dispersion relation in Fig. 5. Overall minima in the dispersion occur at the $(\frac{1}{3}-\delta,\frac{1}{3}-\delta,l)$ and $(\frac{2}{3}+\delta,\frac{2}{3}+\delta,l)$ wave vectors for $l=3n$ and $(\frac{1}{3}+\delta,\frac{1}{3}+\delta,l)$ and $(\frac{2}{3}-\delta,\frac{2}{3}-\delta,l)$ wave vectors for $l=\frac{3}{2}+3n$, where n is an integer and $\delta\approx0.025$. The nonzero value of J_1 results in a finite dispersion along the $(\zeta\ \zeta\ l)$ direction with a periodicity of three reciprocal lattice units (rlu's). This is shown in Fig. 5(b) for the curves plotted using the top axis.

The powder average of the first frequency moment of the $T=0$ energy integrated scattering function,

$$\hbar\langle\omega\rangle_Q \equiv \int_{-\infty}^{\infty}\int \frac{d\Omega d\omega}{4\pi}\hbar\omega(\mathbf{Q})\mathcal{S}(\mathbf{Q},\hbar\omega)$$

$$\propto |F(Q)|^2\left[1-\frac{\sin(Qd)}{Qd}\right],$$

(11)

provides direct information regarding the length of the dimer bond, d. Figure 6 shows the first moment of the measured $T=1.4$ K scattering intensity for both incident wavelengths. These data are fitted to Eq. (11), including an overall constant and a multiplicative prefactor. A simultaneous fit of both data yields a good representation of the measured results with $d=4.073(7)$ Å. This value agrees with the description of the dimer bond being the short vertical bond between Mn^{5+} moments in the $Ba_3Mn_2O_8$ crystal structure $d=3.985$ Å (Fig. 1).
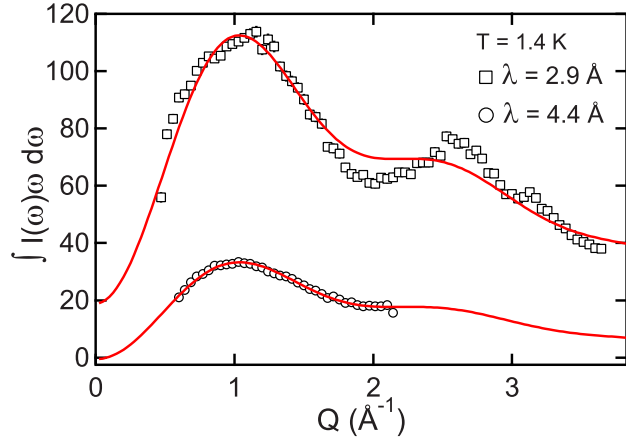
FIG. 6. (Color online) First moment of scattering intensity integrated between $\hbar\omega=0.75$ and 3 meV for the $T=1.4$ K $\lambda=4.4$ and 2.9 Å measurements shown in Figs. 4(a) and 4(b). Solid lines correspond to fits described in the text with the fitted $|\mathbf{d}|$ value of $d=4.073(7)$ Å.

The magnetic spectra of $Ba_3Mn_2O_8$ as a function of temperature for $1.4 < T \leq 160$ K were also measured. In order to consider a range of energy transfers beyond the singlet-triplet band, we examine the $\lambda=2.9$ Å configuration data. Constant wave vector scans for $0.9 \leq Q \leq 1.0$ Å^{-1} are shown in Fig. 7 for several temperatures for both neutron energy gain and
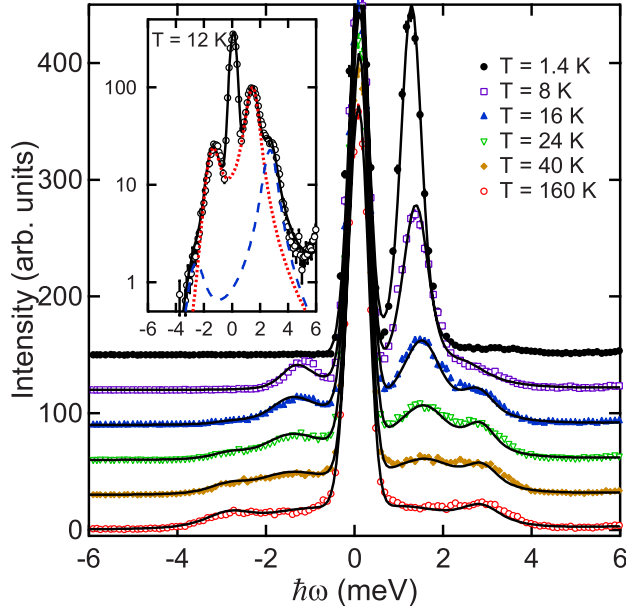

FIG. 7. (Color online) Energy dependent scattering intensity for $0.9 < Q < 1.0$ Å^{-1} for a series of temperatures as measured in the $\lambda=2.9$ Å configuration. Data for different temperatures are vertically offset. Solid lines are fits to the Lorentzian functions described convolved with the energy dependent resolution of the instrument. The inset illustrates scattering intensity of the $T=12$ K measurement plotted on a logarithmic intensity scale. The dotted red line corresponds to the spectral contribution of the lower energy mode, and the dashed blue line corresponds to the higher energy mode.

loss. This wave vector was chosen because it is in the vicinity of both the peak in the density of states and the overall minimum in the measured dispersion. From the $T=1.4$ K spectrum in Fig. 4(b), this wave vector also provides minimal interference from higher energy portions of the singlet-triplet spectrum. The $T=1.4$ K spectrum consists of a single peak at $\hbar\omega \approx 1.25$ meV with no significant scattering intensity on the neutron energy gain side of the spectrum. As temperature is increased, the single peak broadens and moves to slightly larger energy transfers, and additional scattering intensity develops in the vicinity of 3 meV. There is also additional scattering intensity, which develops on the neutron energy gain side of the spectrum at elevated temperatures.

In order to distinguish singlet-triplet and thermally activated triplet-quintet excitations, we model the constant wave vector scans using two excitations. We fit to two Lorentzian functions of the form[33]

$$I(\omega) = \langle n(\omega) + 1\rangle \left(\frac{A\Gamma_1}{(\omega - \omega_1)^2 + \Gamma_1^2} - \frac{A\Gamma_1}{(\omega + \omega_1)^2 + \Gamma_1^2} \right.$$
$$\left. + \frac{B\Gamma_2}{(\omega - \omega_2)^2 + \Gamma_2^2} - \frac{B\Gamma_2}{(\omega + \omega_2)^2 + \Gamma_2^2} \right), \quad (12)$$

where Γ_1, ω_1, Γ_2, and ω_2 are the half-width at half maximum and energy of two respective excitations, with the Lorentzian width reflecting temperature dependent broadening of the spectrum. The Bose factor $\langle n(\omega)+1\rangle \equiv [1 - \exp(-\hbar\omega\beta)]^{-1}$ enforces detailed balance of the scattering intensity. Equation (12) and a variable width and amplitude Gaussian peak at the elastic position were convolved with the energy transfer dependent instrumental energy resolution with fitting parameters A, B, $\Gamma_{1,2}$, and $\omega_{1,2}$. A time independent background of the form $BG \propto (\frac{81.81}{\lambda^2} - \hbar\omega)^{-2}$, as typically used for time-of-flight direct geometry INS measurements, and a constant background were determined from the $T \leq 40$ K data and held fixed. The two excitation fits are shown as solid lines in Fig. 7. The line shapes agree well with the energy dependent distribution of scattering intensity for both neutron energy loss and gain. To further illustrate the presence of the triplet-quintet excitation, we plot the $T=12$ K data and fitted line shape, including the individual contributions from each mode in the inset of Fig. 7.

Figure 8(a) shows the total integrated scattering intensity for both modes as well as the neutron energy gain and loss portions as a function of temperature. We fit the total scattering intensity to the temperature dependent isolated dimer scattering function in Eq. (5) with an overall multiplicative prefactor and the exchange J_0 as fitting parameters. Considering only singlet-triplet excitations yields the dashed red line in Fig. 8(a) and a value of $J_0=3.9(2)$ meV. However, including both singlet-triplet and triplet-quintet modes yields a much better fit (solid black line) and a more appropriate value of $J_0=1.9(3)$ meV. The improved fit implies that there is a non-negligible contribution of thermally activated triplet-quintet excitations at higher energy transfers. The calculated temperature dependent scattering intensity for the neutron energy gain and loss portions of the spectrum based on the
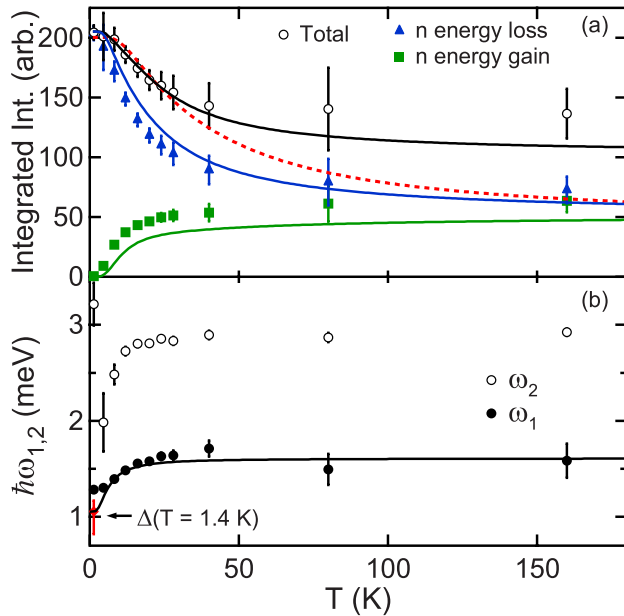
FIG. 8. (Color online) Temperature dependent integrated intensity and characteristic energy determined from fits to data shown in Fig. 7. (a) Total and neutron energy gain and loss portions of the integrated scattering intensity for both modes. The solid black line is a fit of the temperature dependent total scattering intensity of the isolated antiferromagnetic $S=1$ dimer including both singlet-triplet and thermally activated triplet-quintet excitations. The dashed line only includes singlet-triplet excitations. Solid blue and green curves are calculated from the singlet-triplet and triplet-quintet fitted scattering intensity. (b) Mode energy as a function of temperature. The $T=1.4$ K spin-gap value determined from fitted exchange parameters is shown as a single red diamond. The solid line is a calculation of the RPA model temperature dependent spin gap using the determined values of exchange constants.

singlet-triplet, triplet-quintet model also agrees with the data shown in Fig. 8(a).

The fitted values ω_1 and ω_2 are plotted in Fig. 8(b). The ω_1 value is not the spin-gap energy but rather the characteristic energy of the lower energy mode found for the constant wave vector scan. For comparison, we also plot the determined spin-gap energy based on the $T=1.4$ K powder average analysis. The calculated temperature dependent spin gap of the singlet-triplet excitation based on Eqs. (6)–(8) and the fitted exchange constants is plotted as a solid line in Fig. 8(b). The RPA coupled dimer description agrees well with the temperature dependence of the energy scale of the singlet-triplet excitation. We also note that above the base temperature, the RPA function agrees with the temperature dependence of the activated triplet-quintet excitation, ω_2, although shifted to higher energy transfers, implying that these excitations may share a similar temperature dependent dispersion renormalization.

IV. CONCLUSIONS

Through INS measurements, we have shown that a well-defined singlet-triplet spectrum exists in $Ba_3Mn_2O_8$. Although the measured bandwidth of the magnetic spectrum is larger than the spin gap, the exchange constants indicate that $Ba_3Mn_2O_8$ can be considered a triangular lattice of weakly coupled $S=1$ dimers. A comparison to an appropriate RPA coupled dimer description of the scattering function is able to determine the exchange constants. In addition, the wave vector dependent scattering intensity agrees with the dominant dimer bond being the predicted short vertical bond illustrated in Fig. 1(b).

The examination of temperature dependent scattering intensity indicates that both singlet-triplet and triplet-quintet excitations are observed in the INS spectrum (there is no INS cross section for $S=1$ antiferromagnetic singlet-quintet excitations). Based on the relative energy scales of the two observed excitations, we can estimate the mean energy of singlet-quintet excitations as $\approx 3.4(4)$ meV. Single-crystal INS measurements may be able to determine the dispersion associated with thermally activated triplet-quintet excitations or perhaps observe multiparticle excitations, quintet-triplet decay, or interference of single- and multiparticle excitations.[34] The existence of singlet-quintet and triplet-quintet excitations may also be able to explain the heat capacity above $T \approx 3$ K, which cannot be accounted for by single excitation models.[13]

We also point out that the currently determined exchange constants may be able to further describe the magnetic field dependent phase diagram at low temperatures or place limits on the nature of the proposed long-range-ordered phases. The difference between the observed phase diagrams for $H \parallel c$ and $H \perp c$ must be related to the single-ion anisotropy term in the Hamiltonian [Eq. (1)]. As we will show elsewhere,[14] this term induces an effective exchange anisotropy in the low-energy Hamiltonian that results from projecting the original Hamiltonian into the subspace generated by the singlet and $S_z=1$ triplet of each dimer. These two states can be described with a pseudospin $1/2$ variable. The combined effect of geometric frustration and anisotropy leads to the appearance of a new phase for $H \perp c$, which will be discussed in Ref. 14.

[1] J. A. Hertz, Phys. Rev. B **14**, 1165 (1976).

[2] M. Jaime, V. F. Correa, N. Harrison, C. D. Batista, N. Kawashima, Y. Kazuma, G. A. Jorge, R. Stein, I. Heinmaa, S. A. Zvyagin, Y. Sasago, and K. Uchinokura, Phys. Rev. Lett. **93**, 087203 (2004); S. E. Sebastian, N. Harrison, C. D. Batista, L. Balicas, M. Jaime, P. A. Sharma, N. Kawashima, and I. R. Fisher, Nature (London) **441**, 617 (2006).

[3] T. Nikuni, M. Oshikawa, A. Oosawa, and H. Tanaka, Phys. Rev. Lett. **84**, 5868 (2000).

[4] M. B. Stone, I. Zaliznyak, D. H. Reich, and C. Broholm, Phys. Rev. B **64**, 144405 (2001); M. B. Stone, C. Broholm, D. H. Reich, O. Tchernyshyov, P. Vorderwisch, and N. Harrison, Phys. Rev. Lett. **96**, 257203 (2006).

[5] Ch. Rüegg, N. Cavadini, A. Furrer, H.-U. Güdel, K. Krämer, H. Mutka, A. Wildes, K. Habicht, and P. Vorderwisch, Nature (London) **423**, 62 (2003).

[6] A. Zheludev, V. O. Garlea, T. Masuda, H. Manaka, L.-P. Regnault, E. Ressouche, B. Grenier, J.-H. Chung, Y. Qiu, K. Habicht, K. Kiefer, and M. Boehm, Phys. Rev. B **76**, 054450 (2007).

[7] M. B. Stone, C. Broholm, D. H. Reich, P. Schiffer, O. Tchernyshyov, P. Vorderwisch, and N. Harrison, New J. Phys. **9**, 31 (2007).

[8] I. Affleck, Phys. Rev. B **41**, 6697 (1990).

[9] T. Giamarchi and A. M. Tsvelik, Phys. Rev. B **59**, 11398 (1999).

[10] T. M. Rice, Science **298**, 760 (2002).

[11] P. Sengupta and C. D. Batista, Phys. Rev. Lett. **98**, 227201 (2007); **99**, 217205 (2007).

[12] M. Uchida, H. Tanaka, M. I. Bartashevich, and T. Goto, J. Phys. Soc. Jpn. **70**, 1790 (2001).

[13] H. Tsujii, B. Andraka, M. Uchida, H. Tanaka, and Y. Takano, Phys. Rev. B **72**, 214434 (2005).

[14] E. C. Samulon, Y. -J Jo, P. Sengupta, C. D. Batista, M. Jaime, L. Balicas and I. R. Fisher, arXiv:0803.3830.v1 (unpublished).

[15] M. Uchida, H. Tanaka, H. Mitamura, F. Ishikawa, and T. Goto, Phys. Rev. B **66**, 054429 (2002).

[16] S. Hill (private communication).

[17] H.-J. Koo, K.-S. Lee, and M.-H. Whangbo, Inorg. Chem. **45**, 10743 (2006).

[18] M. T. Weller and S. J. Skinner, Acta Crystallogr., Sect. C: Cryst. Struct. Commun. **C55**, 154 (1999).

[19] R. A. Robie and B. S. Hemingway, J. Chem. Thermodyn. **17**, 165 (1985).

[20] G. L. Squires, *Introduction to the Theory of Thermal Neutron Scattering* (Dover, Mineola, NY, 1997).

[21] T. Kato, K. Takatsu, H. Tanaka, W. Shiramura, M. Mori, K. Nakajima, and K. Kakurai, J. Phys. Soc. Jpn. **67**, 752 (1998).

[22] N. Cavadini, W. Henggeler, A. Furrer, H.-U. Güdel, K. Krämer, and H. Mutka, Eur. Phys. J. B **7**, 519 (1999).

[23] N. Cavadini, G. Heigold, W. Henggeler, A. Furrer, H.-U. Güdel, K. Krämer, and H. Mutka, Phys. Rev. B **63**, 172414 (2002).

[24] B. Leuenberger, A. Stebler, H. U. Güdel, A. Furrer, R. Feile, and J. K. Kjems, Phys. Rev. B **30**, 6300 (1984).

[25] B. Leuenberger, H. U. Güdel, and P. Fischer, Phys. Rev. B **33**, 6375 (1986).

[26] Y. Sasago, K. Uchinokura, A. Zheludev, and G. Shirane, Phys. Rev. B **55**, 8357 (1997).

[27] T. Hong, M. Kenzelmann, M. M. Turnbull, C. P. Landee, B. D. Lewis, K. P. Schmidt, G. S. Uhrig, Y. Qiu, C. Broholm, and D. Reich, Phys. Rev. B **74**, 094434 (2006).

[28] P. C. Hohenberg and W. F. Brinkman, Phys. Rev. B **10**, 128 (1974).

[29] S. Ma, C. Broholm, D. Reich, B. Sternlieb, and R. Erwin, Phys. Rev. Lett. **69**, 3571 (1992).

[30] In the absence of an *a priori* calculation of the Mn^{5+} magnetic form factor, we use the calculated Mn^{4+} magnetic form factor as a reasonable approximation.

[31] P. J. Brown, in *International Tables for Crystallography*, edited by A. J. C. Wilson (Kluwer Academic, London, 1995), Vol. C.

[32] Best fit parameters from the overall minimum in χ^2, exchange constant parameter space. Error bars determined by considering fits to the $\lambda = 2.9$ and 4.4 Å measurements for the range of exchange parameters corresponding to the respective χ^2 values up to $1.05\chi^2_{min}$.

[33] I. A. Zaliznyak, L.-P. Regnault, and D. Petitgrand, Phys. Rev. B **50**, 15824 (1994).

[34] M. B. Stone, I. A. Zaliznyak, T. Hong, D. H. Reich, and C. L. Broholm, Nature (London) **440**, 187 (2006).